



UV and visible light optimization of anatase TiO₂ antimicrobial properties: Surface deposition of metal and oxide (Cu, Zn, Ag) species



Anna Kubacka*, Mario J. Muñoz-Batista, Manuel Ferrer, Marcos Fernández-García*

Instituto de Catálisis y Petroleoquímica, CSIC, C/Marie Curie 2, 28049 Madrid, Spain

ARTICLE INFO

Article history:

Received 7 March 2013

Received in revised form 22 April 2013

Accepted 30 April 2013

Available online 9 May 2013

Keywords:

Titania

Anatase

Silver, copper, zinc, oxides, biocide

Germicide

Disinfection

ABSTRACT

Presence of metallic Ag or oxidic Ag, Cu and Zn species on an anatase surface is shown to allow drastic modification of the disinfection capability of TiO₂-based materials against both Gram-negative (*Escherichia coli*) and Gram-positive (*Staphylococcus aureus*) bacteria and upon both ultraviolet and visible light excitations. While Cu shows non-positive influence in the photo-elimination of the microorganisms, Zn and Ag always displays an improved performance with respect to the bare titania reference. In particular, Zn has a positive effect with decreasing importance with increasing wavelength whereas Ag always display an optimum performance, irrespective of the initial oxidation state, excitation wavelength and microorganism nature. The physico-chemical analysis of the samples together with a spectro-kinetic combination based in a Langmuir-Hinshelwood-like kinetic model and the use of electron paramagnetic resonance were utilized to analyze the roots of the mentioned Cu, Zn, Ag dependent disinfection behavior. The approach allows the critical analysis of the effects that the metal-containing phases exert in anatase and provides evidence that two physical phenomena are of importance to justify the disinfection capability modification of the anatase phase. Both adhesion to bacteria and hole-radical derived attack to the microorganism appear critical to interpret disinfection although their relative contribution vary with the excitation light wavelength as well as the nature of the metal-containing phase present at the anatase surface.

© 2013 Elsevier B.V. All rights reserved.

1. Introduction

TiO₂-Anatase is by far the most widely used photocatalyst, being a wide band-gap (3.0–3.2 eV) semiconductor that under illumination generates energy-rich electron-hole pairs able to generate chemistry and/or degrade cell components of microorganisms [1–3]. After the seminal works of Matsunga and co-workers [4,5] the biocide capability of anatase has been the subject of a large number of studies summarized in recent reviews [see, for example, [6–8]. In short, TiO₂ appears as a relatively new biocidal agent with significant advantages over conventional ones due, in first place, to the (relative) innocuousness of the material for humans, and, on second hand, to the absence of known weaknesses concerning the type of organism (Gram-positive and Gram-negative bacteria, viruses and fungi) [1,6,9–11]. Improvement of anatase materials is actively sought not only to obtain better antimicrobial materials but also to overcome the limited absorbance power of anatase in the visible light electromagnetic region and, therefore, the scarce potential to use renewable energy sources as the

sun and/or the possibility of using visible-light indoor sources for supplying energy to photokilling processes.

Among the paths previously studied to optimize biocidal properties of anatase, modification by surface deposition of metallic silver is a well known tool allowing both enhanced charge separation by metal electron capture as well as promoting visible absorption (in the 450–550 nm range) through the localized metal surface plasmon (LSP) [12–24]. Moreover, dark activity has been mentioned frequently due to direct contact of the nanocomposite material with the microorganism and/or silver release to the media. The Ag–TiO₂ system is consider among the most potent and long lasting antimicrobial agents as a result of the harmonic combination of the properties of the two components of the material [1,6,7,25]. On the other hand, the oxide-anatase contact has been also tested with a significant number of systems in the context of biological decontamination [1,2,6,9]. Among them, AgO_x [26–28], CuO_x [18,29–31] and ZnO [32–34] appear optimum choices for separating charge carrier upon both UV and visible light (Ag, Cu, even Zn [35]), and thus to facilitate the subsequent charge carrier attack to the microorganisms. Similarly to Ag–TiO₂, the Cu- or Zn–TiO₂ materials possess antimicrobial properties, either under light or at dark conditions, originated independently from both components of the nano-composite material and may be thus systems with high potential [6,29–35].

* Corresponding authors. Tel.: +34915 85 4939; fax: +34 915 85 47 60.

E-mail addresses: ak@icp.csic.es (A. Kubacka), mfg@icp.csic.es, m.fernandez@icp.csic.es (M. Fernández-García).

In this work we explored these four surface-doped anatase-TiO₂ materials in the photoelimination of two microorganisms, a Gram-negative (*Escherichia coli*) and a Gram-positive (*Staphylococcus aureus*) bacterium. We observed the promotion of TiO₂ activity in the cases of Zn and Ag while Cu displays a modest worsening of the biocidal properties of the bare oxide. This is interpreted with the help of a complete characterization of fresh and used materials as well as from the light shed by a spectro-kinetic approach. A kinetic modeling of the results was carried out following the work of Marugan et al. [36]. Modeling of the inactivation profiles is grounded in a simplified (Langmuir–Hinshelwood-like multistep-type) reaction mechanism and considers that microorganism death occurs via a sequential attack of photo-radicals by which “undamaged” cells become “damaged” and eventually progress to an “inactivated” state. As previously noted, the utilization of an “adsorption Langmuir–Hinshelwood” type mechanism allows a reasonable and relatively flexible description of the inactivation. Moreover, the advantage of using this approach appears two-fold: first, (i) its usefulness in analyzing complete sets of inactivation profiles showing (or lacking) initial smooth/fast decays and final tailing section; and, additionally, (ii) the model renders kinetic parameters allowing physical interpretation of the underlying process, in contraposition with many other simple kinetic laws used previously [6,36,37]. To support the results of the model, electron paramagnetic resonance (EPR) studies of the charge carrier formation were conducted. Data on charge species behavior was correlated with disinfection rates obtained from the kinetic model. With this approach we aim to spot out differences among the metal-containing samples and interpret them on physical basis.

2. Experimental

2.1. Catalysts preparation

The TiO₂ component was prepared using a microemulsion synthetic route and calcined at 723 K for 2 h as detailed previously in ref. [38]. Using this material, silver was photo-deposited from an aqueous solution of silver nitrate (Merck) to a content of 1 wt.% (metal basis) without further treatment. Ag, Cu and Zn nitrate precursors (Merk) to a content of 1 wt.% (metal basis) were also used within a wet impregnation method and calcined at the same temperature than TiO₂. Samples are called Ti (bare metal), Cu, Zn and Ag for calcined samples and Ag(ph) for the photodeposited one. Chemical analyses and BET areas for the materials are presented in Table 1.

2.2. Catalysts characterization

The BET surface areas and average pore sizes were measured by nitrogen physisorption (Micromeritics ASAP 2010). XRD profiles were obtained with a Seifert D-500 diffractometer using Ni-filtered Cu K α radiation with a 0.02° step and fitted using the Von Dreele approach to the Le Bail method [39]; particle sizes and microstrain were measured with XRD using the Williamson–Hall formalism [40]. UV–vis diffuse reflectance spectroscopy experiments were

performed with a Shimadzu UV2100 apparatus. XPS data were recorded on 4 mm \times 4 mm pellets, 0.5 mm thick, prepared by slightly pressing the powered materials which were outgassed in the prechamber of the instrument at room temperature up to a pressure $< 2 \times 10^{-8}$ to remove chemisorbed water from their surfaces. The SPECS spectrometer main chamber, working at a pressure $< 10^{-9}$ Torr, was equipped with a PHOIBOS 150 multi-channel hemispherical electron analyzer with a dual X-ray source working with Ag K α ($h\nu = 1486.2$ eV) at 120 W, 20 mA using C 1s as energy reference (284.6 eV). Surface chemical compositions were estimated from XP-spectra, by calculating the integral of each peak after subtraction of the “S-shaped” Shirley-type background using the appropriate experimental sensitivity factors and the CASAXPS (version 2.3.15) software. Ag, Cu and Zn lixiviation after reaction was analyzed by using inductive coupled plasma-ICP (Perkin-Elmer, Optima 3300 DV).

The electron paramagnetic resonance (EPR) measurements were done with a Bruker ER200D spectrometer operating in the X-band and calibrated with a DPPH standard. For the 5,5-dimethyl-1-pyrroline N-oxide (DMPO) spin trapping EPR experiments, the samples were suspended in water (at a concentration of 0.6 g L⁻¹) and were sonicated for 4 min. An aqueous solution (0.01 M) of DMPO spin trap (supplied by Sigma) was prepared and kept on ice during the whole set of experiments. Bidistilled water (Elix-10) was employed for these preparations. 100 μ l of the solid suspension and 100 μ l of the DMPO solution were mixed into an EPR flat quartz cell under atmospheric air and irradiated at different times, through a spectroscopic Pyrex glass filter with a cut-off at ca. 220 nm, with light excitation source identical to that employed for the photokilling tests (280/500 nm), being then immediately transferred to the spectrometer cavity for EPR analysis. A small radical concentration decay (of ca. 5% on average) was observed in the dark during the course of spectrum recording. The latter were obtained at 298 K at ca. 9.75 GHz microwave frequency, 19.5 mW microwave power, 100 kHz modulation frequency, 1 G modulation amplitude and 2×10^5 spectrometer gain. No significant signal saturation was observed in those conditions. Blank experiments were also performed over mixtures of 100 μ l of the DMPO solution and 100 μ l of water to check the absence of radical formation in the absence of solid under the employed conditions.

2.3. Microbiological tests

The microorganisms used in this study include *E. coli* 1337-H and *S. aureus* 1341-H and were obtained from the German Collection of Microorganisms and Cell Cultures (DSMZ, Braunschweig, Germany) and cultured and maintained according to the recommendations of the suppliers [41]. Briefly, *E. coli* 1337-H and *S. aureus* 1341-H were grown in Luria–Bertani (LB) medium at 37 °C using 100 mL flasks filled with 10 mL of the medium and subsequently used for photochemical cell viability assays. To study the antimicrobial activity of films, a suspension containing 10 μ l of microbial cells (ca. 10⁹ cell forming units (CFU) mL⁻¹) suspended in 1 mL broth solution was made [42]. Aliquots of 1 ml from these suspensions were added to a 4 mL quartz cubic cell containing 1 ml of sterilized water and the corresponding film under continuous stirring and oxygen supply. The slurry (at a previously optimized concentration of 0.6 g L⁻¹) was placed in the UV spectrometer chamber (Synergy HT Multi-Mode Microplate Reader - BioTek) and irradiated with a light at 280 (UV) and 425/500 (visible) nm for different time periods. The excitation linewidth is lower than 10 nm in all cases.

The five samples (Ti and Ag(ph), Ag, Cu and Zn containing nanocomposites) together with blank tests (using either light without catalyst or the materials at dark conditions) were measured using the same bacterium inoculums (8.9×10^8 CFU mL⁻¹)

Table 1
Main characterization results for metal-containing and TiO₂ reference systems.

Sample	M atomic percentage (%) ^a	BET surface area (m ² g ⁻¹)
Ti	–	87.1
Cu	0.97	74.8
Zn	1.02	75.6
Ag	0.98	80.1
Ag(ph)	1.01	83.8

^a ICP-AAAs; standard error: 3%.

for each microorganism tested. Excitation was carried with an UV-visible spectrometer (UNIKON 930) equipped with filters to obtain monochromatic radiation (10 nm half width). As demonstrated by blank experiments, care was put of using a sub-lethal, maximum radiation energy fluence of ca. 1 kJ m^{-2} throughout the study. After irradiation and for different time intervals, aliquots of $100 \mu\text{L}$ were transferred to a 10 mL LB broth test tube. The order of cell dilution at this stage was 10^{-2} . Loss of viability after each exposure time was determined by the viable count procedure on LB agar plates after serial dilution (10^{-2} to 10^{-5}). All plates were incubated at 37°C for 24 h after which they were scanned using a Bio-Rad Imaging System equipped with Analysis Software 4.6.5 (Bio-Rad) to enable enumeration of bacterial colonies among replicates. Data reported in this contribution are typically the average of four different experiments. A minimum of four experimental runs was performed to determine antimicrobial activity; this leads to a standard error below $\pm 0.01 \text{ log CFU ml}^{-1}$ units in the reported results.

2.4. Kinetic modeling

Modeling of the inactivation profiles was achieved, as mentioned, using an approach grounded in a simplified (Langmuir–Hinshelwood-like multistep-type) reaction mechanism based in three parameters; kinetic (k) and pseudo-adsorption (K) constants and an inhibition coefficient (n) [36]. The model considers that microorganism death occurs via a sequential attack of photo-radicals by which “undamaged” (denoted as u in subsequent equations) cells become “damaged” (denoted as d) and eventually progress to an “inactivated” state [6,36]. This leads to two differential equations as:

$$\frac{dN_u}{dt} = -k \frac{KN_u^n}{1 + KN_u^n + KN_d^n}$$

$$\frac{dN_d}{dt} = k \frac{KN_u^n - KN_d^n}{1 + KN_u^n + KN_d^n}$$

We modified this model by assuming a fast decay from “undamaged” to inactivated cells which would lead to a simplified mechanism with a single differential equation paralleling the one of a classical Langmuir–Hinshelwood mechanism:

$$\frac{dN_u}{dt} = -k \frac{KN_u^n}{1 + KN_u^n}$$

Numerical solution of the corresponding set of equations was achieved with a 5th order “adaptive size controlled” Runge–Kutta program, coupled to a Full Newton (non-linear fitting) algorithm in order to ensure the solution of the corresponding non-linear fitting problem [43]. Results reported here, e.g. in the specific reaction conditions used, concern the second model (single differential equation) as a better fit is obtained as judged by the coefficient of determination R^2 . Note nonetheless the trends among the catalysts series using both models were the same, indicating that interpretation of the results are independent of the model.

Table 2
XRD-derived parameters for the anatase phase of the samples.^a

Sample	Size (nm)	Microstrain $\langle \epsilon^2 \rangle^{1/2}$	Cell parameters (Å)		Cell volume (Å ³)
			$a = b$	c	
Ti	11.3	0.0010	3.785	9.478	135.8
Cu	12.1	0.0019	3.789	9.472	136.0
Zn	12.8	0.0022	3.790	9.475	136.1
Ag	12.5	0.0021	3.789	9.472	136.0
Ag(ph)	11.9	0.0018	3.790	9.469	136.0

^a Standard errors: 12% (size), 10% (strain), $\pm 0.004 \text{ Å}$ (cell parameters), 0.2% (cell volume).

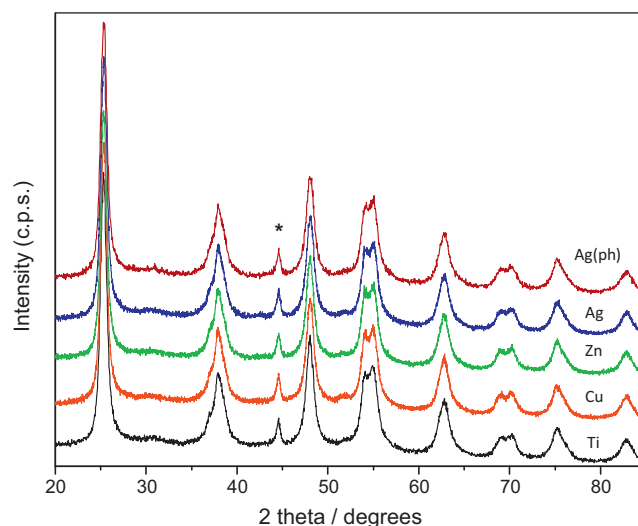


Fig. 1. XRD patterns for metal-containing and TiO_2 samples. The asterisk indicates a peak coming from sample holder.

3. Results and discussion

Fig. 1 displays the XRD patterns of the samples. All samples showed the anatase structure (JCPDS card 78-2486, corresponding to the $I41/amd$ space group) with structural/morphological characteristics summarized in Table 2. The presence of metal-containing phases in the TiO_2 -based materials does not alter the structural characteristics of the anatase phase, as justified by the near-constancy of cell parameters and volume throughout the series of samples analyzed. Nevertheless, they tend to favor a modest increase of the particle size as well as of the microstrain, the later due to the increase of the surface contribution [44]. The effect of metal surface species in modifying anatase particle size and strain during calcination has been previously analyzed, with Cu and Zn highlighted as cations which facilitate the growth of the oxide particle size [45].

Concerning the oxidation state of the cations [46] the XPS study indicates the exclusive presence of Ti(IV) with a $2p_{3/2}$ binding energy at $458.25 \pm 0.3 \text{ eV}$ for all samples. The chemical state of the surface metal-containing phases was also analyzed using XPS. Representative spectra are shown in Fig. 2 while a summary of relevant observables from XPS is presented in Table 3. Cu and Zn present characteristic Cu(II)/Zn(II) oxidation states, although the irradiation reduces Cu in the XPS measurement chamber, as evidenced by both the significant intensity decrease of the shake-up peak and the shift to lower binding energies of the 2p doublet structure (Fig. 2). The Cu oxidation state was further confirmed with UV–vis spectroscopy (see below). In the case of silver and in agreement of expectations from the preparation method procedures followed, we observed the presence of dominant Ag(0) and AgO phases for, respectively, the Ag(ph) and Ag samples. So, a dominant metallic state is observed for the photodeposited sample while full

Table 3XPS results for metal-containing and TiO₂ reference samples. Observable values are given with the number of significant figures.

Sample	BE _{Ti} (eV)	BE _{Ag 3d5/2} (eV)	BE _{Cu 2p3/2} (eV)	BE _{Zn 2p3/2} (eV)	M/Ti	M/Ti _(XPS)
Ti	458.6	–	–	–	–	–
Cu	458.3	–	932.05	–	0.013	0.023
Zn	458.1	–	–	1021.3 ₅	0.012	0.024
Ag	458.5	367.5	–	–	0.007 ₅	0.009
Ag (ph)	458.5	368.3	–	–	0.007 ₅	0.012

oxidized states are observed for Cu, Zn and Ag after calcination [46,47]. Table 3 also gives information concerning the dispersion state of the samples. Cu and Zn present a more aggregate state than both Ag-containing samples. Comparing M/Ti ideal (100% dispersed state) and real ones would indicate that, roughly, Cu and Zn have a dispersion value about one fourth lower than those of the Ag and Ag(ph) samples.

Fig. 3 presents the UV–vis spectra of the samples. The optical spectra of M–TiO₂ materials are dominated by the anatase band gap around 380 nm [47,48]. Analysis of the band gap assuming an indirect gap semiconductor (like the bulk anatase material) indicates the constancy of the band gap energy within experimental error (ca. 0.03 eV). The result provides evidence that, as previously described with XRD, Ag, Cu and Zn species are essentially at the surface of the anatase component, with practical absence of any doping process of this structure. Fig. 3 also indicates the presence of the Ag–LSP at ca. 550 nm in the Ag–TiO₂ nanoparticles. This points out the metallic state of silver [12], in agreement with XPS results. The optical spectra (Fig. 3) also indicate that the Cu(II) species already detected by XPS has limited size and local order characteristic of pseudo-octahedral positions. Such size-limited centers produce electronic states near the anatase conduction band (at the absorption edge in the figure) as well as d–d characteristic transition with maximum at ca. 800 nm [29,48,49]. Oxidized Zn, as expected and due to its large band gap energy, does not modify appreciable the UV–vis spectra of the anatase material (we recall that metals at the inorganic component are in a composition of 1 wt.%) [32–34].

Interesting to note is that as judged by XPS (not shown) and UV–vis (Fig. 3) the systems does not suffer significant evolution under reaction conditions expect in the case of Ag(ph). As can be seen in Fig. 3B, the initial, dominant metallic state evolves into a AgO-type oxidic state without practical differences with the Ag-calcined sample. This happens upon all light energies tested. This behavior has been previously observed [13] and indicates the relatively minor effect of the preparation step in the final chemical state of silver. Note that this is not general case and, particularly, for lower and higher Ag contents, the metal-oxide interaction and the “size” protection of a stable Ag(0) metallic core under reaction conditions affect, respectively, the final oxidation state of silver [12,13].

Summarizing the characterization results, we founded that samples show relatively dispersed phases onto the anatase surface. The anatase phase only shows minimal differences among samples; this concerns structural and electronic (particularly optical) properties of the nano-composite samples. Calcined samples display in all cases a M(II) oxidation state while the photo-reduced sample evolved from a zero valent state to a M(II) state. Relatively minor differences are encountered among samples in respect to the surface dispersion degree of the metals. Electronically, the band gap of titania remains unaltered in presence of such metals and only localized d–d Cu transitions (of secondary importance from the view point of the photocatalytic process) are observed as localized-type states in the visible region of the electromagnetic spectrum.

Results for the photoelimination of the model Gram-negative (*E. coli*) and Gram-positive (*S. aureus*) bacteria are presented in Fig. 4. Such figure does not display blank experiments as they showed

the absence of killing (less than 0.4 log CFU ml^{−1} at the end of the experiment) due to the very low irradiation power used in the experiments. This has been discussed in larger detail by the authors for similar experiments [50–53]. Dark activity was only observed for Ag cases (below 1.1 log units at the end of experiment). This is further discussed below. As a general description of the experimental results presented in Fig. 4, we note an apparent improved performance under UV than visible light for all samples tested, with relatively little influence of the nature of the microorganism. Fig. 4 shows that presence of Copper seems detrimental or, at least, non-positive for the biokilling action displayed by the titania reference while silver-containing samples seem to display the best performance in all cases tested, irrespective of light energy and microorganism nature. The general landscape to interpret the biocidal behavior presented in Fig. 4 for M-containing materials is discussed at length below.

To this end Fig. 4 also presents results for the modeling work. As previously noted, the utilization of an “adsorption Langmuir–Hinshelwood” type mechanism allows a reasonable and relatively flexible description of the inactivation profiles. Of course, the complexity of the photo-activated disinfection process occurring once a microbe is in contact with a photogenerated radical means that we can talk of a “adsorption Langmuir–Hinshelwood” type mechanism where the complex set of elemental steps describing the process is crudely approximated. Still the model allows us to qualitatively differentiate between the relative importance of the adhesion and the radical attack processes (see below). The presence of initial shoulders (inexistent under UV and only weakly detected under visible excitation for Ti and Cu cases) and/or tailing final regions is evident in the majority of cases under study in Fig. 4. The fitting results also displayed in Fig. 4 provide evidence of the goodness of the models which adequately describe the experimental data, including the mentioned initial shoulders and/or final tailing regions. It may be however noted that the model is not able to completely describe tailing regions in a single case (UV-light; Ag(ph) sample). In spite of this, rather high values, above 0.999, of the coefficient of determination *R*² are obtained in all cases.

Metal-containing phases at the surface of anatase can play several roles in the reaction. These roles have been previously unveiled by several works [1,6,7,9,10,12,13] and will be here evaluated separately with the help of a combined analysis of the disinfection process using kinetic modeling and EPR. Results in Fig. 4 would indicate that Cu does not improve TiO₂ performance while Zn and particularly Ag make an important positive effect. Differences among Ag-containing samples are modest, as expected by their similar physico-chemical characteristics. To interpret the situation, we must first recall here that the metal-containing titania interaction present in our 1 wt.% samples is enough to limit significant lixiviation. Calibration curves for Cu, Zn and Ag indicate that within the reaction time, a maximum of 2% of the metal(s) content will leave the material surface, eliminating this from the list of the possible noble metal roles concerning the optimization of the disinfection activity in our experiments.

Our titania-anatase has (surface) basic character [54] and a relatively high point of zero charge (also called isoelectric point, IE). An IE point near or above 7 (e.g., basic character) is required to

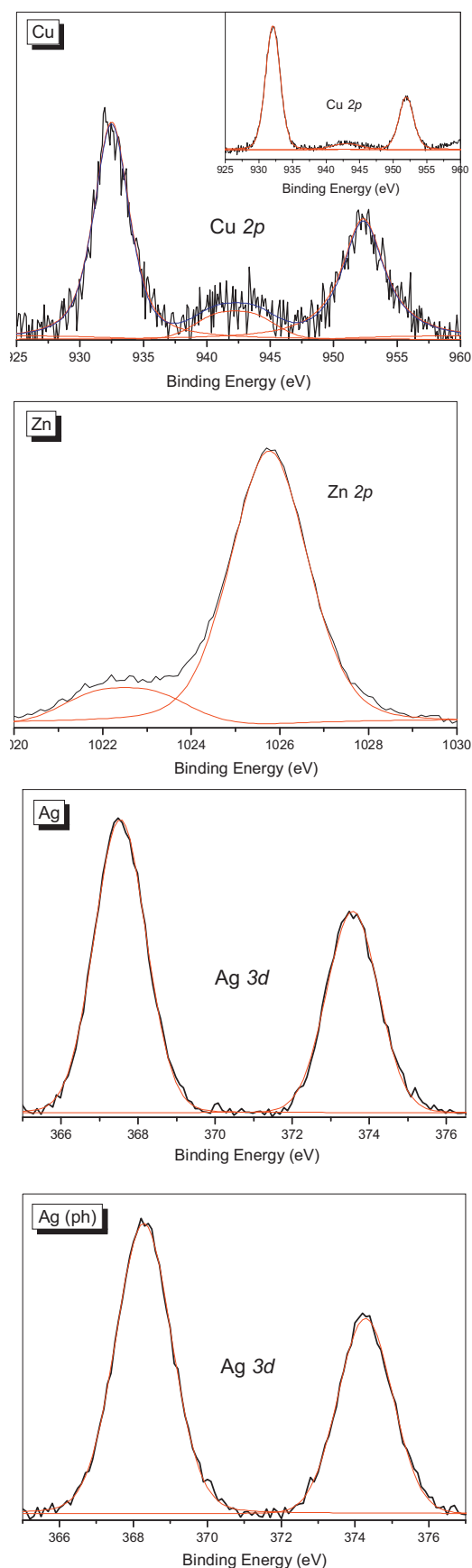


Fig. 2. Cu 2p, Zn 2p and Ag 3d XPS spectra for the doped-samples. In the copper case we show the initial (fast recording) and final (normal time recording) spectra. See text for details.

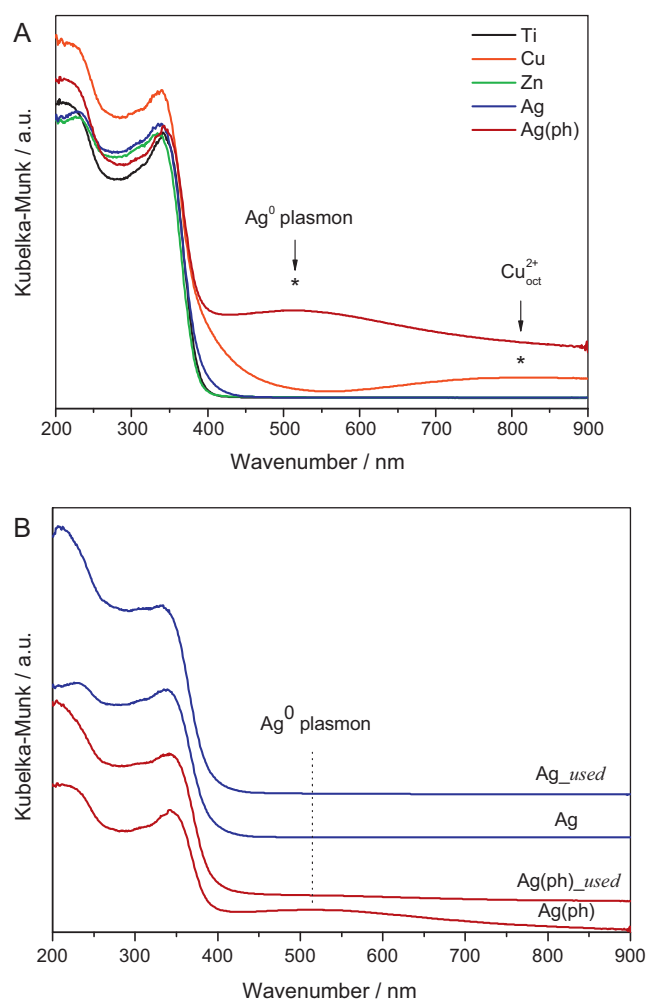


Fig. 3. UV-vis spectra for metal-containing and TiO₂ samples (A) fresh samples; (B) used samples (scaled up for easy comparison).

have optimum *E. coli* inactivation [55]. Our (maximum) metal content is too low to allow detection of significant IE changes (below 15%) with respect to our titania support. As reported, only loadings ca. 5 wt.%, can drive to measurable variations in the point of zero charge (PZC), altering in this way the initial steps of the microorganism interaction (adhesion) to the catalyst surface [56]. Nevertheless, the metal-containing phases presumably influence the surface adhesion properties of the system by affecting the properties of anatase at a local level. This point is here analyzed with the help of the adsorption constants obtained from the modeling of the inactivation curves (Fig. 5; middle panels). Adhesion of the bacteria has been shown to be an important step of the reaction [10,57]. We can see that the adsorption constant behaves in a different way for UV (280 nm) and visible (425/500 nm) excitation. This is qualitatively explained by two facts: i) modification of catalyst surface by effect of light (e.g. super-hydrophilicity), and ii) all metals are passive or active optical phases for, respectively, UV and visible light, modifying the electro-dynamic state of the surface. Ag and Cu phases are optically active upon visible light, allowing the absorption of visible light, while in the case of Zn the active states are essentially interface state [26–35]. So, while under UV we observed a trend like $\text{Cu} \leq \text{Ti} \leq \text{Zn}$, Ag, Ag(ph), under visible light the trend is different at 425 nm $\text{Ti} \approx \text{Cu} \geq \text{Zn} \approx \text{Ag}$, Ag(ph) or 500 nm $\text{Ti} \approx \text{Cu} \leq \text{Zn} \geq \text{Ag}$, Ag(ph). In short, less important variations under visible than UV light and a different order of samples can be observed by modifying the energy of the light. Relatively minor

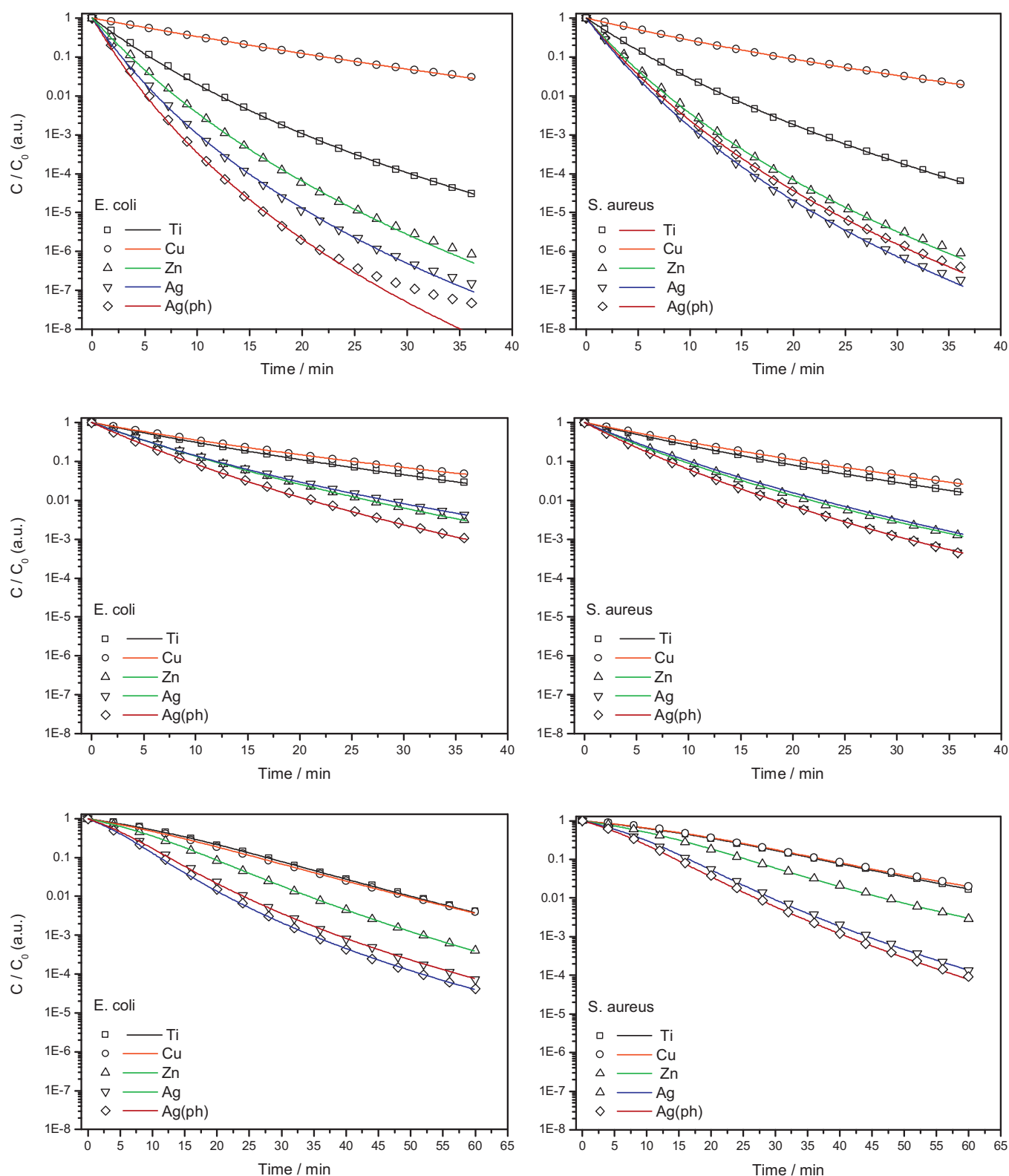


Fig. 4. Elimination profiles (scattered data) and kinetic modeling (dash line) for Gram-negative (*E. coli*) and Gram-positive (*S. aureus*) bacteria under 280 (upper panels), 425 (middle panels) and 500 (lower panels) nm light excitation. Note the different time scale.

differences appear as a function of the microorganism nature; most apparent being just observed for trends observed after Zn under UV light (Fig. 5, middle panels).

The kinetic constant behavior through the sample series is presented in Fig. 5. The disinfection process occurred with significant

activity both under visible and UV light excitations, albeit at much lower extent in the former. This fact is clearly reflected in the corresponding kinetic constant values. The plot in Fig. 5 (upper panels) also provides evidence that bacterial killing is promoted by some of the surface metal-containing species here analyzed, independently

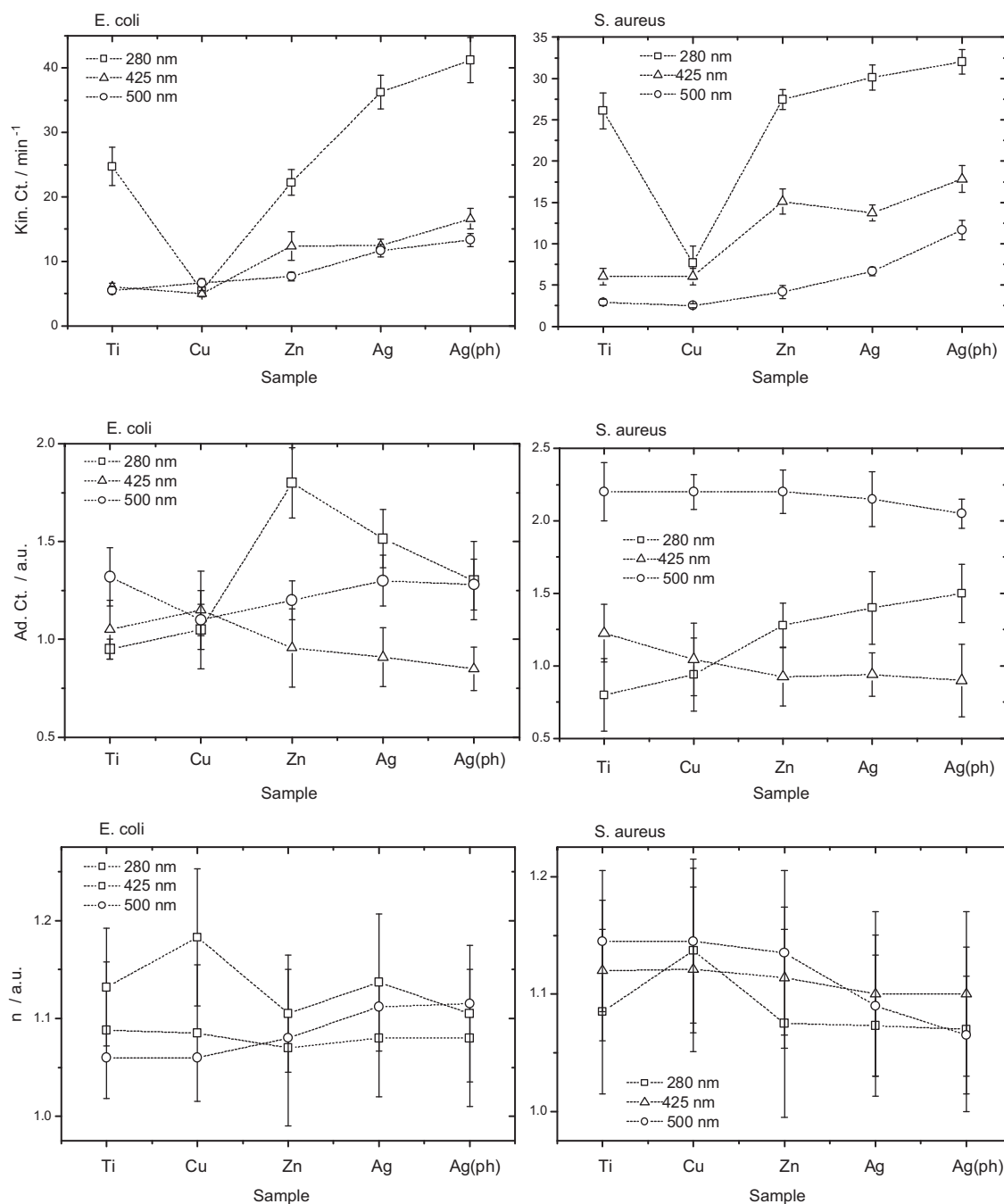


Fig. 5. Kinetic and adsorption constants and exponent coefficients obtained from the kinetic analyses displayed in Fig. 4.

if model Gram-negative or Gram-positive bacteria are used in the experiment. Although differences between the two microorganisms tested are relatively modest, higher kinetic constant seems to be generally obtained for *E. coli* vs. *S. aureus*. This is in accordance with the better performance generally observed for Gram-negative vs. Gram-positive bacteria inactivation in photo-catalytic disinfection processes. Such observation is primarily justified in the fact that these two classes of bacteria differ considerably in cell membrane structure (different composition of lipids and proteins) [6,7]. The latter is without doubt a key issue in the disinfection process, although recent studies indicate a more general effect, not only based in the specific physico-chemical (e.g. oxidation) modification suffered by the membrane but additionally related to drastic genetic shifts such as regulation and replication caused at very

low levels of active photo-radical species and thus of potential importance even at the very early stage of the photokilling process [10,11,18].

Before discussing in detail the kinetic constant results displayed in Fig. 5, we analyzed the formation of radicals with EPR. As noted in the literature, there is strong and conclusive evidence that OH radical attack is the responsible of the inactivation process both under UV [6,13,58–60] and visible [6,60,61] light excitations. Only in cases where this path is not allowed, oxygen-related radicals will be dominantly involved in the process. This would occur typically with anion doped TiO₂ samples [62]. A detailed analysis of the TiO₂-surface OH groups responsible for radical creation by other than EPR techniques is not an easy task as, for example, IR would not selectively study hydroxyl groups involved in radical generation

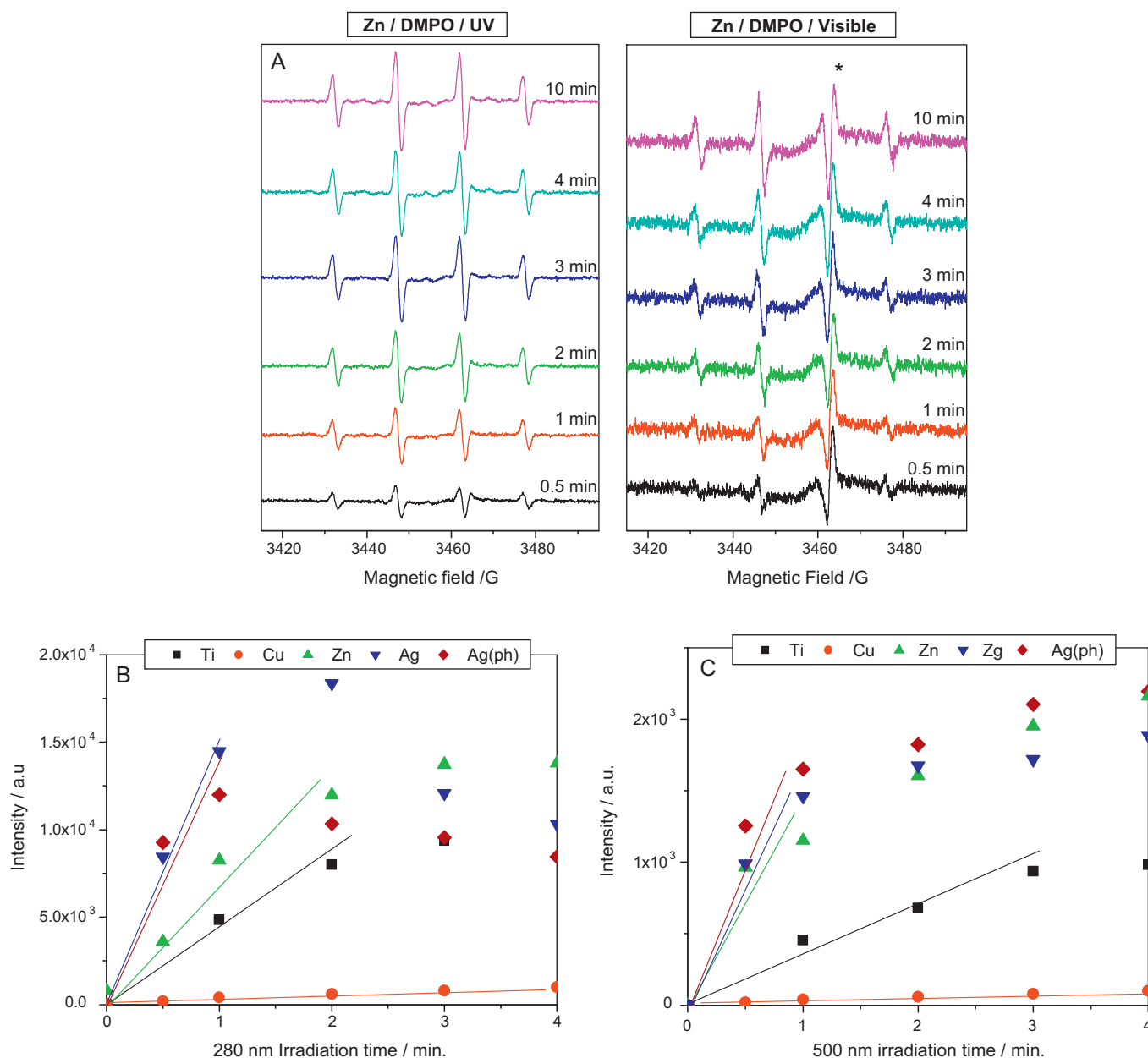


Fig. 6. (A) EPR spectra under UV and visible light irradiation of the DMPO-OH signal obtained after different time contact in presence of the Zn material. The asterisk mark the cavity signal in the case of a weak contribution from the sample (B and C) Evolution of the DMPO-OH signal intensity for the samples studied as a function of irradiation time for, respectively, 280 and 500 nm excitation energy. Lines correspond to the initial slope for OH radical formation.

upon light absorption. A measure of the holes trapped at the material surface and involved in the microorganism inactivation can be thus obtained through the quantification of OH radicals using EPR. UV irradiation of DMPO-containing sample suspensions gives rise to a signal with 1:2:2:1 intensity pattern for all samples (Fig. 6A). Its EPR parameters ($g = 2.0056$, $a_N = 14.9$ G, $a_H = 14.9$ G) are characteristic of DMPO-OH adducts. The accumulation of DMPO-OH radical adducts grows continuously in all cases but such radicals have a limited stability and a maximum concentration as a function of time is always detected. The latter is an effect of multiple additions, within consecutive reactions, of OH radicals to DMPO molecules to yield diamagnetic species [63–66]. Comparison of samples should be thus carried out on the basis of the OH-radical initial formation rate.

The intensity of the DMPO-OH adduct signal as a function of the time is plotted in Figs. 6B and C for, respectively, UV (280 nm) and

visible (500 nm) light excitation. All samples, except Cu, showed a maximum at relatively short times. This may be expected as CuO is the only phase among the studied ones which, according to the valence/conduction band positions, can withdraw holes from the anatase phase [2]. The others metal-containing phases are able to capture and accumulate electrons [2,35,67]. This drives to a simple interpretation upon UV. Upon visible light excitation the situation is more complex as either two phases (in the case of the Cu- and Ag-containing samples, the corresponding nano-oxides and the nanosized TiO₂ which contains localized gap states) or for Zn, the Zn-Ti interface [35] and, at least, the nano-TiO₂ phase, are optically active and can absorb photons. The distribution of charge carriers among the existing phases is thus more complex to be predicted when visible radiation is used in the excitation of the samples. In any case, although, according to their relative valence/conduction band positions with respect to TiO₂, all Cu, Zn and Ag-containing

(oxidized) phases are potentially able to improve charge separation and thus charge available at anatase surfaces, nevertheless one of them, Cu, would subtract the active hole-related species from the mentioned anatase surface [2]. The intensity plots are in full agreement with this simple, theoretical prediction. The lines included in Fig. 6B/C are related to the initial behavior of the samples and their slope defines the initial OH-radical formation rate. From Fig. 6B/C we can then observed a UV tend like $\text{Cu} \ll \text{Ti} < \text{Zn} \ll \text{Ag}$, Ag(ph) and a visible (500 nm) one like $\text{Cu} \ll \text{Ti} \ll \text{Zn}$, Ag , Ag(ph) . The Cu detrimental effect is confirmed irrespective of the excitation light wavelength while the other metal-containing phases show a positive effect which magnitude has a visible dependence with the light wavelength.

More importantly, the EPR analysis and Fig. 7 provide conclusive evidence of the strong correlation observed between the initial rate for OH-radical formation and the inactivation kinetic constants obtained from the modeling presented in Fig. 5. While several characteristic regions appear to exist both under UV and visible excitation, a linear-type correlation is observed in all of them. The different regions are likely related to differences among samples concerning ($\text{MO}_x\text{-TiO}_2$ interface) physico-chemical parameters like interaction area–dispersion of MO_x , electronic contact and others. Together with the mentioned differences concerning Cu and other metals (in turn related to the charge handling at interfaces which drives to hole/electron withdraw from Ti by Cu/others and pointing out the origin of the singular Cu behavior in the plot) would explain the general trends observed in Fig. 7. So, in spite of the complex interpretation of details contained in Fig. 7, the strong correlation observed between the two observables plotted corroborates that the trend extracted from the kinetic constants (Fig. 5) has physical meaning and thus provide a good (yet qualitative) background to interpret the differential (in this case, respect to anatase) disinfection capability of the samples. We stress the fact that the model does not pretend to interpret the biocidal behavior in an absolute scale but just to give useful insights into the differential behavior taking TiO_2 as reference. Such a rationalizing tool would thus provide a powerful tool to validate the kinetic analysis carried out, in turn assessing (vide supra) the scientific background of the biocidal behavior along the series of samples analyzed.

So, considering the kinetic constants presented in Fig. 5, a relatively similar general trend of the observable among the sample's series is observed irrespective of the microorganism nature. This occurs in both cases, upon UV and visible light excitation. The most marked difference concerns the Cu behavior upon UV and visible

excitation and may be related, as above mentioned, with the fact that the hole handling in this system may differ from UV to visible excitation as the phase where they (the hole-related charge carriers) are dominantly formed is, respectively, anatase or copper oxide. Note that both hole-related species are known to produce chemistry although it is well established that those reaching the surface of TiO_2 are significantly more efficient [2]. The different formation of the hole-related radicals would strongly affect their fate (particularly their recombination as well as their potential to interact with the microorganism) but the general outcome is that the TiO_2 performance level is never reached in presence of Cu at the surface, irrespective of the light energy. To summarize, trends presented in Fig. 5 (upper panels) are $\text{Cu} < \text{Ti} \leq \text{Zn} \leq \text{Ag}$, Ag(ph) for UV light and $\text{Ti} \approx \text{Cu} < \text{Zn} \leq \text{Ag}$, Ag(ph) for all visible light energies tested (425/500 nm).

To justify the inactivation curves it is therefore obvious that adhesion and charge carrier (more concretely hole-related carriers directly involved in disinfection) properties are important. Other possible effects related to lixiviation or to surface-poisoning seem secondary. The latter is quantified within our kinetic analysis by the inhibition coefficient (n), graphically displayed in Fig. 5(lower panels). This parameter accounts for the inhibition produced by the increasing concentration of cell debris and oxidation products appearing toward the end of the experiment and competing strongly for the radical species effectively eliminating microorganism [6,36]. The n coefficient is inherently higher than 1 and the larger the difference from this value the acute is the inhibition phenomenon. Fig. 5 shows inhibition coefficients around 1.1 with relatively small differences (less than 7.5%) among samples, irrespective of the microorganism and energy of excitation light. This suggests that the influence of a self-poisoning effect in our disinfection tests is relatively moderate and, moreover, that it does not influence to a large extent the differential behavior of the samples with respect to the TiO_2 reference.

So, focusing attention in the two more important factors to rationalize photo-induced disinfection in TiO_2 based nanomaterials, the relative importance of adhesion and OH-related radical attack factors varies from UV to visible light and less markedly with the nature of the microorganism. In particular, we first discuss the UV case. Trends presented for the adsorption and kinetic constants are, respectively, $\text{Cu} \leq \text{Ti} \leq \text{Zn}$, Ag , Ag(ph) and $\text{Cu} < \text{Ti} \leq \text{Zn} \leq \text{Ag}$, Ag(ph) . Note that UV performance corresponds to the situation most affected by the microorganism nature; differences among the sample's series behavior are nevertheless constrained to trends of adsorption constants after Zn (Fig. 5, middle panels). In spite of it, an essentially harmonic trend is observed for the two (adsorption and kinetic) constants and thus the final result is that Cu does not favor the disinfection capability of our reference Ti sample but all other surface metal-containing phases improve the photo-killing behavior of the reference. Both factors, adhesion and hole attack to the microorganism, seem important in attaining an improved performance with respect to the bare anatase material while using UV excitation.

For visible light we observed differences in adsorption constant trends at 425 and 500 nm for samples going from Zn to Ag(ph) . In fact the trends observed for all constants were $\text{Ti} \approx \text{Cu} \geq \text{Zn} \approx \text{Ag}$, Ag(ph) (425 nm adsorption ct.), $\text{Ti} \approx \text{Cu} \leq \text{Zn} \geq \text{Ag}$, Ag(ph) (500 nm adsorption ct.) and $\text{Ti} \approx \text{Cu} < \text{Zn} \leq \text{Ag}$, Ag(ph) (425/500 nm kinetic ct.). So, while Cu displays a similar performance than Ti, the (modest) positive influence of the kinetic constant for the remaining (Zn, Ag) samples is partially counteracted by the adsorption constant at 425 nm while at 500 nm both (adsorption and kinetic) constants display similar trends (more concretely, improved – kinetic constant- or negative/quasi-constant – adsorption constant at 425/500 nm-behavior with respect to the TiO_2 reference). Zn and Ag would thus improve the performance of TiO_2 from

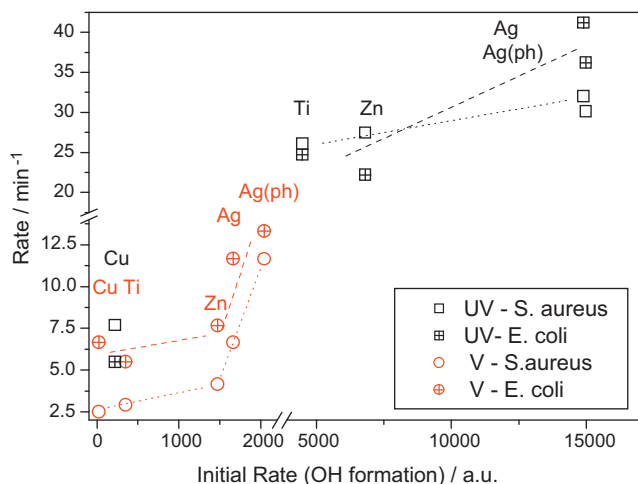


Fig. 7. Correlation plot between the initial rate of OH radical formation and kinetic constants presented in Fig. 5 for UV (280 nm) and visible (500 nm) excitation energy.

400 to 500 nm by wavelength-dependent factors, mostly based, as mentioned, in the corresponding dependence of the adsorption constant behavior. Although variations of the adsorption constants with respect to the TiO₂ reference are relatively modest for all cases upon visible light, they would be based, as mentioned previously, in potential differences in local surface properties of the anatase phase around the metal-containing entities. Local (subtle) modification of the surface charge but also hydrophobicity [11,57,68] as a function of excitation wavelength can be here invoked to justify this result. The different, wavelength-dependent charge distribution and/or hydrophobicity (both in turn related to the metal-containing electronic properties as well as OH-radical nature/quantity) near metal-containing surface sites would thus be key to interpret the behavior. Such hypothesis cannot be fully analyzed at the moment as would require in situ experiments with vibrational or other spectroscopic tools which would discern between bacteria adsorbed in different surface sites of the material. This has not been carried out and is possibly out of current technical capabilities.

Finally, it can be noted that some differences seem evident concerning the behavior of the most efficient (e.g. those leading to activity increase) Zn and Ag cations at anatase surfaces. Zn has a relatively different effect upon UV or visible light excitation. This would be justified in the different electronic properties of the ZnO phase itself and the Ti–Zn interface states (e.g., the corresponding “optically-active” phase in constant with TiO₂ for, respectively, UV and visible light). So, under UV we observed a modest or negligible positive effect on the kinetic contact together with a more significant positive influence on the adsorption constant. Upon visible light, the biocidal activity improvement of Zn (with respect to the TiO₂ reference) is less significant than under UV (and less important as the excitation wavelength grows) and mostly based in an increase of the kinetic constant. For Ag-containing samples the behavior is always dominated by the contact between the Ag and Ti containing (oxide) phases and the subsequent interface charge handling and drives to an increase in the kinetic constants for all visible-light excitation wavelengths here analyzed. This appears the dominant factor in the boosting of activity and a unique characteristic of the Ag-containing materials.

4. Conclusions

Four metal-containing TiO₂-based samples were analyzed in terms of their photo-killing disinfection against Gram-negative (*E. coli*) and Gram-positive (*S. aureus*) bacteria. The relative behavior with respect to the bare anatase reference was interpreted through a complete characterization of the fresh and used catalysts as well as from the light shed by a spectro-kinetic approach.

While Cu shows non-positive influence on the anatase photo-disinfection of microorganisms, Zn and Ag display a positive influence. In particular, Zn has an overall or net positive effect with a moderate, decreasing magnitude with increasing excitation wavelength (from UV to visible) whereas Ag optimizes photo-killing activity of anatase irrespective of the initial oxidation state and irradiation wavelength. Detail analysis indicates that (differential–among samples with respect to a TiO₂ reference system) disinfection results here presented are not affected by either lixiviation of cations at metal-containing surface phases or by any (differential) self-poisoning effect originated from cell debris produced during the disinfection process. Differences among samples seem affected by two phenomena: adhesion of the materials to the cells as well as cell inactivation/death by OH-related radical attack. The constant non-positive effect of Cu in anatase performance

seems a direct consequence of the Cu effect on hole generation as evidenced by EPR upon both UV and visible light excitation. The positive effects of Zn and Ag seem on the other hand wavelength dependent. Upon UV and in presence of these two cations, adhesion and OH-radical attack phenomena both improve (e.g. increase of corresponding adsorption and kinetic constants) with respect to the TiO₂ reference. The relative importance of these two factors seems however different for Zn and Ag. In the 400–500 nm (visible) range we also observed a Zn or Ag-related increase in OH-radical formation with respect to TiO₂ but the adhesion phenomena would display a wavelength-dependent behavior not fully understood at the moment.

Acknowledgements

A. Kubacka and M.J. Muñoz-Batista acknowledge MINECO for support thought, respectively, the postdoctoral “Ramón y Cajal” and predoctoral FPI programs. Financial support by MINECO is also acknowledged (CTQ2010-14872/BQU, PLE2009-0037, PRPPRI-PIBJP-2011-0914).

References

- [1] O. Carp, C.L. Huisman, A. Reller, Photoinduced Progress in Solid State Chemistry 32 (2004) 33.
- [2] A. Kubacka, G. Colón, M. Fernández-García, Chemical Reviews 112 (2012) 1555.
- [3] M. Peláez, N.T. Nolan, S.C. Pillai, M.K. Severy, P. Falaras, A.G. Kontos, P.S.M. Dunlop, J.A. Bryne, D.D. Dionysiou, Applied Catalysis B 125 (2012) 331.
- [4] T. Matsunga, R. Tamada, H. Wake, FEMS Microbiology Letters 20 (1985) 211.
- [5] J.C. Ireland, P. Klostermann, E.W. Rice, R.M. Clark, Applied and Environment Microbiology 53 (1993) 1668.
- [6] O.K. Dalrymple, E. Stefanakos, M.A. Trozt, D.Y. Goswamy, Applied Catalysis B 98 (2010) 27.
- [7] P.S.M. Dunlop, C.P.S. Sheeran, J.A. Bryne, M.A.S. McMahon, M.A. Boyle, K.G. McGuigan, Journal of Photochemistry and Photobiology A 216 (2010) 303.
- [8] M.A. Mahmood, S. Baruah, A.K. Anal, J. Dutta, Environmental Chemistry Letters 10 (2012) 145.
- [9] R. Vinu, G. Madras, Journal of the Indian Institute of Science 90 (2010) 189.
- [10] H.A. Foster, I.B. Ditta, S. Varghese, A. Steele, Applied Microbiology and Biotechnology 90 (2011) 1847.
- [11] N.J. Sucher, M.C. Carles, J. Nowotny, T. Bak, Advances in Applied Ceramics 111 (2012) 16.
- [12] P.V. Kamat, Journal of Physical Chemistry C 111 (2007) 2834.
- [13] A. Kubacka, M. Ferrer, A. Martínez-Arias, M. Fernández-García, Applied Catalysis B 84 (2008) 87.
- [14] R. van Grieken, J. Marugan, C. Sordo, P. Martínez, C. Pablos, Applied Catalysis B 93 (2009) 112.
- [15] R. Vinu, G. Madras, Applied Catalysis A 366 (2009) 130.
- [16] Q. Zhang, C. Sun, Y. Zhao, X. Hu, P. Chen, Environmental Science and Technology 44 (2010) 8270.
- [17] D. Wodka, E. Bielska, R.P. Socha, I. Kumari, ACS Applied Materials & Interfaces 2 (2010) 1945.
- [18] H.A. Foster, D.W. Sheel, P. Sheel, P. Evans, S. Varghese, N. Eutschke, H.M. Yates, Journal of Photochemistry and Photobiology A 216 (2010) 283.
- [19] T.-T. Tsai, W.-P. Sung, W. Song, Environmental Engineering Science 28 (2011) 635.
- [20] I. Medina-Ramirez, Z. Luo, S. Bashir, R. Mernaugh, J.L. Liu, Dalton Transactions 40 (2011) 1047.
- [21] R.G. Nair, J.K. Roy, S.K. Samdarshi, A.K. Mukherjee, Colloids and Surfaces B: Biointerfaces 86 (2011) 7.
- [22] K. Kowal, K. Wysocka-Król, M. Kopaczynska, E. Dworniczek, R. Franciczek, M. Wawrzyńska, M. Vargová, H. Podbielska, Journal of Colloid and Interface Science 362 (2011) 50.
- [23] L. Liu, Z. Liu, H. Bai, D.D. Sun, Water Research 46 (2012) 112.
- [24] J. Zhang, X. Liu, S. Gao, B. Huang, Y. Dai, Y. Xu, L.R. Grabstanowicz, T. Xu, Ceramics International 39 (2013) 1011.
- [25] L. Liu, B. John, K.L. Yeung, Journal of Environmental Sciences 21 (2009) 700.
- [26] Q. Chen, C. Li, V. Paulinek, P. Sahara, H. Wang, Applied Surface Science 252 (2006) 4154.
- [27] E. Pullido Melián, O. González Díaz, J.M. Doña Rodríguez, G. Colón, J.A. Navío, M. Macías, J. Pérez Peña, Applied Catalysis B 127 (2012) 112.
- [28] M. Grandcolas, J. Ye, N. Hanagata, Materials Letters 65 (2001) 236.
- [29] M.K.I. Senevirathna, P.K.D.D.P. Pitigala, K. Tennakone, Journal of Photochemistry and Photobiology A 171 (2005) 257.
- [30] A. Torres, C. Ruales, C. Pulgarín, A. Aimable, P. Bowen, V. Sarria, J. Kiwi, ACS Applied Materials & Interfaces 2 (2010) 2547.
- [31] C. Karunakaran, G. Abiramar, P. Gomathisankar, G. Manikandan, V. Anandi, Journal of Colloid and Interface Science 352 (2010) 68.
- [32] D. Chen, H. Zhang, S. Hu, J. Li, Journal of Physical Chemistry C 112 (2008) 117.

- [33] C. Karunakaran, G. Abiramar, P. Gomathisankar, G. Manikandan, V. Anandi, *Materials Research Bulletin* 46 (2011) 1586.
- [34] S.H. Hwang, J. Song, Y. Jung, O.Y. Kweon, H. Song, J.H. Jang, *Chemical Communications* 47 (2011) 9164.
- [35] X. Yang, C. Zhou, X. Gao, W. Gao, *Journal of Materials Chemistry* 22 (2012) 5629.
- [36] J. Marugán, R. van Grieken, C. Sordo, C. Cruz, *Applied Catalysis B* 82 (2008) 27.
- [37] A. Kubacka, M. Ferrer, A. Martínez-Arias, M. Fernández-García, *Applied Catalysis B* 121–122 (2012) 230.
- [38] M. Fernández-García, X. Wang, C. Belver, J.C. Hanson, J.A. Rodríguez, *Journal of Physical Chemistry C* 111 (2007) 674.
- [39] A. Le Bail, H. Duroy, J.L. Forquet, *Materials Research Bulletin* 23 (1988) 447.
- [40] G.K. Williamson, W.H. Hall, *Acta Metallurgica* 1 (1953) 22–31.
- [41] J. Sambrook, E.F. Fritsch, T. Maniatis, *Molecular Cloning: A Laboratory Manual*, 2nd ed., Cold Spring Harbor Laboratory Press, Cold Spring Harbor, 1989.
- [42] M. Ferrer, J. Soliveri, F.J. Plou, N. López-Cortés, D. Reyes-Duarte, M. Christensen, J.L. Copa-Patiño, A. Ballesteros, *Enzyme and Microbial Technology* 36 (2005) 391.
- [43] J.E. Dennis, D.M. Gay, R.E. Welsh, *ACM Transactions on mathematical Software* 7 (1981) 348–369.
- [44] L.E. Depero, L. Sangaletti, B. Allieri, E. Bontempi, A. Marino, M. Zocchi, *Journal of Crystal Growth* 198–199 (1999) 516.
- [45] M. Fernández-García, A. Martínez-Arias, J.C. Hanson, J.A. Rodríguez, *Chemical Reviews* 104 (2004) 4063.
- [46] C.D. Wagner, W.M. Riggs, L.E. Davis, J.F. Moulder, in: G.E. Muilenber (Ed.), *Handbook of X-ray Photoemission spectra*, Perkin-Elmer, Minnesota, 1976.
- [47] A. Kubacka, M. Fernández-García, G. Colón, *Journal of Catalysis* 254 (2008) 272.
- [48] H. Irie, K. Kamiya, T. Shibamura, S. Miura, D.A. Tryk, T. Yokohama, K. Hashimoto, *Journal of Physical Chemistry C* 113 (2009) 10761.
- [49] J.J. Bravo-Suarez, B. Subramanian, R. Vahaudhai, *Journal of Physical Chemistry C* 116 (2012) 18207.
- [50] A. Kubacka, C. Serrano, M. Ferrer, H. Lünsdorf, P. Bielecki, M.L. Cerrada, M. Fernández-García, M. Fernández-García, *Nano Letters* 7 (2007) 2529.
- [51] M.L. Cerrada, C. Serrano, M. Sánchez-Chaves, F. Fernández-Martín, A. de Andrés, R. Jiménez-Riobóo, M. Fernández-García, A. Kubacka, M. Ferrer, M. Fernández-García, *Advanced Functional Materials* 18 (2008) 1949.
- [52] A. Kubacka, M. Ferrer, M.L. Cerrada, M. Sánchez-Chaves, M. Fernández-García, A. de Andrés, R.J.J. Riobóo, M. Fernández-García, *Applied Catalysis B* 89 (2009) 441.
- [53] A. Kubacka, M. Ferrer, M. Fernández-García, C. Serrano, M.L. Cerrada, M. Fernández-García, *Applied Catalysis B* 104 (2011) 346.
- [54] C. Adán, A. Martínez-Arias, M. Fernández-García, A. Bahamonde, *Applied Catalysis B* 76 (2007) 395.
- [55] D. Gummy, C. Morris, P. Bowen, C. Pulgarin, S. Giraldo, R. Hazdun, J. Kiwi, *Applied Catalysis B* 63 (2006) 76.
- [56] A. Di Paola, E. García-López, G. Marci, C. Martin, L. Palmisano, V. Rives, A.M. Venezia, *Applied Catalysis B* 4 (2004) 223.
- [57] B. Li, B.E. Logan, *Colloids and Surfaces B* 36 (2004) 81.
- [58] M. Cho, H. Chung, W. Choi, J. Yoon, *Journal of Water Research* 38 (2004) 1069.
- [59] A. Vohra, D.Y. Goswami, D.A. Deshpande, S.S. Block, *Applied Catalysis B* 66 (2006) 57.
- [60] G. Verak, L. Manczinger, G. Bozau, A. Sienkiewicz, L. Forró, K. Maogyorosi, K. Hernadi, A. Dombi, *Applied Catalysis B* 129 (2013) 566.
- [61] J.C. Yu, W. Ko, J. Yu, H. Yip, P.K. Wong, J. Zhao, *Environmental Science and Technology* 29 (2005) 1175.
- [62] J.A. Renglifo-Herrera, K. Pierzchola, A. Sienkiewicz, L. Forró, J. Kiwi, C. Pulgarin, *Applied Catalysis B* 88 (2009) 398.
- [63] M.D. Hernández-Alonso, A.B. Hungría, A. Martínez-Arias, M. Fernández-García, J.M. Coronado, J.C. Conesa, J. Soria, *Applied Catalysis B* 50 (2004) 167.
- [64] M.A. Grela, M.E.J. Coronel, A.J. Colussi, *Journal of Physical Chemistry* 100 (1996) 16940.
- [65] E.G. Janzen, N. Sankuraty, Y. Kotake, *Journal of Magnetic Resonance* 111 (1996) 254.
- [66] D. Dvoranova, V. Brezova, M. Mazur, M.A. Malati, *Applied Catalysis B* 37 (2002) 91.
- [67] J.C. Conesa, *Journal of Physical Chemistry C* 116 (2012) 18884.
- [68] C. Pablos, R. van Grieken, J. Marugán, I. Chowdury, S.L. Walker, *Catalysis Today* 209 (2013) 140, <http://dx.doi.org/10.1016/j.cattod.2012.12.010>.